

<https://doi.org/10.1038/s43246-024-00455-x>

# Electric-field-aligned liquid crystal polymer for doubling anisotropic thermal conductivity



Maohua Li<sup>1,2,3,6</sup>, Ping Gong<sup>2,6</sup>, Zhenbang Zhang<sup>2</sup>, Linhong Li<sup>2</sup>, Yapeng Chen<sup>2</sup>, Yue Qin<sup>2,4</sup>, Yingying Guo<sup>1</sup>, Rongjie Yang<sup>2</sup>, Jianxiang Zhang<sup>2</sup>, Yiwei Zhou<sup>2</sup>, Kang Xu<sup>2</sup>, Yandong Wang<sup>2</sup>, Hainam Do<sup>4</sup>, Xiaofei Jia<sup>5</sup>, Tao Cai<sup>2</sup>, Cheng-Te Lin<sup>2,3</sup> & Jinhong Yu<sup>2,3</sup>

High thermal conductive polymers have become more important because equipment requires high performance, high-energy density, and high integration. There are different strategies to make high thermal conductive polymers, among which is the synthesis of polymers in the liquid crystal phase. However, the thermal conductivity of such material is rarely beyond  $1 \text{ W m}^{-1} \text{ K}^{-1}$  because of the disordered molecular directionality. The disordered directionality between crystal zones limits the thermal conductivity in a specific direction. Here, we show a method for unifying the direction of crystal zones by applying an external electric field on the liquid crystal monomers. Meanwhile, by exposing the transparent equipment and specially designed photopolymerisable monomer in UV light, the liquid crystal monomer is in situ polymerised into a liquid crystal polymer with a high intrinsic thermal conductivity of  $1.02 \text{ W m}^{-1} \text{ K}^{-1}$ . The molecular alignment was characterised and resulted in the resultant high conductivity.

With the rapid development of the electronic industry, there is an increasing emphasis on the miniaturisation and high-energy density of devices, highlighting the importance of heat management. The inadequate dissipation of heat poses a threat to the security and stability of electronic systems. As a result, significant efforts have been made to enhance the thermal conductivity of materials, particularly polymer-based composites, which are extensively used as packaging materials in the electronics industry.

Generally, composites are composed of fillers and a matrix. In thermal conductive composites, the fillers include graphene, carbon fibre, boron nitride, etc., while the matrix is made of polymer<sup>1–8</sup>. Usually, the thermal conductivities of these fillers exceed  $100 \text{ W m}^{-1} \text{ K}^{-1}$ , which is 2 to 4 orders of magnitude higher than that of bulk polymers<sup>9</sup>. Effective methods to achieve thermally conductive composites include using fillers with high thermal conductivity, aligning the thermally conductive direction of the fillers, or increasing the filler loading. However, the resulting thermal conductivities of these composites are typically 1 to 2 orders of magnitude lower than the

intrinsic value of the fillers. This is partly due to the inherently low thermal conductivity of polymers, which is generally below  $0.5 \text{ W m}^{-1} \text{ K}^{-1}$ . Despite this fact, it is challenging to replace polymers due to their unique mechanical and processing properties. Thus, much effort has been devoted to achieving high thermal conductive polymers<sup>10</sup>.

Two major strategies are commonly employed to address this challenge<sup>11</sup>. The first one involves stretching polymer chains to achieve their alignment in a designated direction. In theory, the substance of heat is the thermal motion of atoms, and the atomic bonding dramatically affects the speed of heat transport. When the polymer chain is aligned in a specific direction, heat can be transported along the polymer chain where atoms are connected with a covalent bond<sup>12,13</sup>. In 2013, Cahill et al. measured the axial thermal conductivity of polymer fibres with time-domain thermoreflectance (TDTR). They pointed out that the axial thermal conductivity of polymer reaches several tens of  $\text{W m}^{-1} \text{ K}^{-1}$ , significantly higher than the thermal conductivity of bulk polymers<sup>14</sup>. Gang et al. reported a method of manufacturing polymer nano-fibre with thermal conductivity high to

<sup>1</sup>Qianwan Institute of CNITECH, 315336 Ningbo, Zhejiang, China. <sup>2</sup>Key Laboratory of Marine Materials and Related Technologies, Zhejiang Key Laboratory of Marine Materials and Protective Technologies, Ningbo Institute of Materials Technology and Engineering (NIMTE), Chinese Academy of Sciences, 315201 Ningbo, China. <sup>3</sup>Center of Materials Science and Optoelectronics Engineering, University of Chinese Academy of Sciences, 100049 Beijing, China. <sup>4</sup>Department of Chemical and Environmental Engineering, University of Nottingham Ningbo China, 315100 Ningbo, China. <sup>5</sup>Key Laboratory of Optic-electric Sensing and Analytical Chemistry for Life Science, MOE, College of Chemistry and Molecular Engineering, Qingdao University of Science and Technology, 266042 Qingdao, China.

<sup>6</sup>These authors contributed equally: Maohua Li, Ping Gong. e-mail: [jiangnan@nimte.ac.cn](mailto:jiangnan@nimte.ac.cn); [yujinhong@nimte.ac.cn](mailto:yujinhong@nimte.ac.cn)

$104 \text{ W m}^{-1} \text{ K}^{-1}$ , which is comparable with metal<sup>15</sup>. Another significant development in this field was the bulk production of high thermal conductive polymers, proposed by Gang et al. in 2019<sup>16</sup>. In that work, polymer chains were drawn to form the aligned lamina. The authors illustrated the alignment of polymer lamina with wide-angle X-ray scattering (WAXS) and explained the relationship between the escalating thermal conductivity and the alignment. The highest thermal conductivity achieved in the work reaches  $62 \text{ W m}^{-1} \text{ K}^{-1}$ . Subsequently, the high thermal conductive polymer fibre was widely used in composites as a thermal conductive filler<sup>17–19</sup>. However, one of the challenges faced by this strategy is how to combine polymer with thermal conductive fillers, as the presence of fillers may disrupt the alignment of the polymer. Currently, drawn polymer fibres are primarily used as thermal conductive fillers in organic thermal conductive composites, taking the place of inorganic fillers.

The other strategy involves using liquid crystal polymers (LCPs)<sup>20–22</sup>. Scientists envision that the self-assembly of liquid crystal segments constructs a directional thermal highway and that the crystal structure of LCPs can partially mitigate phonon scattering in amorphous polymer chains. Different from the first strategy, synthesising LCPs from monomers generates block polymers instead of nanofibers or films, so in implementing this method, fillers can be used regardless of their sizes<sup>23–25</sup>. In 1993, Hammerschmidt et al. reported the thermal conductivity of liquid crystalline diacrylates. The reported thermal conductivity along polymer chain orientation is higher than  $5 \text{ W m}^{-1} \text{ K}^{-1}$ , while on the perpendicular direction, this value is only  $0.33\text{--}0.34 \text{ W m}^{-1} \text{ K}^{-1}$  (see ref. 26). This result indicates the anisotropic thermal conductivity of liquid crystal and implies the value of aligning liquid crystal molecular on adjusting thermal conductivity. After that, the thermal conductivity of different liquid crystals, the thermal conductivity difference between phases and the influence of soft segments on thermal conductivity were characterised<sup>27–30</sup>. Due to the liquid crystal's responsiveness to electromagnetic fields, additional fields have been applied to the polymer to regulate thermal conductivity<sup>31,32</sup>. By applying organic chemical vapour deposition on polymer, Gang et al. achieved the enhancement of both covalent bonding along the polymer chain and the  $\pi$ - $\pi$  stacking non-covalent interaction between different chains and raised the intrinsic thermal conductivity of a polymer to  $2 \text{ W m}^{-1} \text{ K}^{-1}$  (see ref. 33). Similarly, in Gu and co-workers' work, liquid crystalline polyimide and various thermal conductive materials were combined to prepare thermal conductive composites<sup>10,30,34</sup>. It should be noted that not all thermal conductive polymers can be used as the matrix compositing with filler, so the influence of these works should be underlined. In other research, liquid crystal was employed as a thermally conductive coupling agent to enhance the heat transport of different polymers and composites by introducing hydrogen bonds<sup>23,35–37</sup>. All these applications and research demonstrated the potential of LCPs, but the measured thermal conductivity of LCPs has rarely been beyond  $1 \text{ W m}^{-1} \text{ K}^{-1}$ . Meanwhile, in most cases, LCPs were aligned parallel to the substrate, also known as the in-plane direction. This causes high thermal conductivity in the in-plane direction and low thermal conductivity in the through-plane direction (perpendicular to the in-plane direction)<sup>38</sup>.

Liquid crystal materials are highly responsive to external fields, making them indispensable in various fields as anisotropic materials. Moreover, extensive research efforts have been dedicated to unravelling the various motion behaviours of liquid crystals in an electric and magnetic field<sup>39–41</sup>. These studies make it possible to align liquid crystals with an external field in the direction where high thermal conductivity is required.

In this study, we introduced an electric field to control the alignment of liquid crystal acrylic acid monomers, which were then photopolymerised into LCPs to enhance their thermal conductivity. This approach allowed for precise control of the arrangement of the liquid crystal molecules, optimising the thermal conduction pathways and improving the thermal transport properties. Different methods were applied to prove the alignment of the molecular chains, and the influence on the thermal properties was analysed. The results of this work demonstrate that by introducing an

electric field for controlling liquid crystal polymers, we can effectively improve their thermal conductivity, opening up new possibilities for applying LCPs in thermal management.

## Results and discussion

### Confirmation of structure

The synthetic routes for the liquid crystal polymer PBPE-C3-AA are depicted in Fig. 1a, while the experimental details of the synthesis process are described in the experiment section. The precursors and monomers were characterised using NMR, as shown in Fig. 1b. It was found that the four doublets located at 7–8.5 ppm were assigned to four hydrogen atoms on diphenyl and benzene. In contrast, the three peaks at 4.17, 3.59 and 1.91 ppm were assigned to the six hydrogen atoms on the aliphatic chain consisting of three carbon atoms. The first two peaks were triplets, while the last one was a multiplet, demonstrating that the peak located at 1.91 ppm should be assigned to the hydrogens on the middle carbon. In the NMR spectrum of BPE-C3-AA, the three peaks located at 6.35, 6.20 and 5.96 ppm were assigned to three hydrogen atoms on the acrylic ester. The splitting pattern once again helped to analyse the assignment of each peak. Specifically, the peak at 6.20 ppm was found to be a quartet, indicating that the hydrogen atom is adjacent to a carbon atom with two other hydrogen atoms that experience a different chemical environment. The other two peaks were doublets, which confirmed the assumption above. Moreover, the chemical shift of the hydrogen atoms on the aliphatic chain increased due to the change in the chemical environment. The degree of influence depended on the distance between the hydrogens and the acrylic acid. In addition, the  $^{13}\text{C}$ - $^1\text{H}$  2D nuclear magnetic resonance spectroscopy results are displayed in Fig. 1c.

The FTIR spectra of the monomers and precursors are displayed in Fig. 1d. In the FTIR spectrum of BPE, the peak at  $3414 \text{ cm}^{-1}$  indicates the presence of a -OH functional group on the precursor. After reacting with 3-chloro-1-propanol, BPE was connected with an aliphatic chain, so the C-H stretching vibration of the aliphatic chain was observed in the FTIR spectrum at  $2900\text{--}3000 \text{ cm}^{-1}$ . Furthermore, the -OH functional group was replaced by an ether, which links the benzene and the aliphatic chain, and its infrared absorption was also observed in the FTIR spectrum of BPE-C3 at  $1051 \text{ cm}^{-1}$ . In addition, the monomer's spectrum exhibited an infrared absorption at  $1407 \text{ cm}^{-1}$ , which can be assigned to the C=C stretching vibration of acrylic ester. 2D-IR were taken in different ranges and shown in Fig. 1e to analyse the interaction between various functional groups. Peaks at  $1509$  and  $1604 \text{ cm}^{-1}$  are assigned to the in-plane bending of C-H and symmetric stretching of the C-C bond on benzene. Their correlated vibration can be found on the synchronous spectrum. Meanwhile, peaks at  $1005$  and  $1052 \text{ cm}^{-1}$  are assigned to the bending vibration combination of benzene and symmetric stretching of the C-O bond of ester. Their correlated vibration can only be found on the synchronous spectrum, indicating their interaction.

MS was used to confirm the chemical structure of the monomer, as shown in Fig. 1f. In MS, the maximum  $m/z$  is 651, which is precisely the molecular weight of the monomer, and the chips represented by 233, 303 and 361 peaks were also drawn as inset. All these methods were powerful methods to identify chemicals. So far, the structures of the monomer and its precursors can be confirmed.

### Crystallisation of monomer and polymer

The liquid crystal properties of the monomer were confirmed through a combination of DSC and polarising microscope observations. DSC measurements revealed that the melting temperature and liquid crystal-to-isotropic phase transition temperature were  $101.8$  and  $160.2^\circ\text{C}$ , respectively (see Fig. 2a). Polarising microscopy allowed for further observation of the phase changes that occurred between these two transition temperatures. As shown in Fig. 2b, c, a droplet of the monomer was observed at temperatures both lower than and beyond  $101^\circ\text{C}$ . When the temperature is beyond  $101^\circ\text{C}$ , it can be found that the colour transformation of the samples is smoother. Meanwhile, the sample shows colour consistency on a larger scale

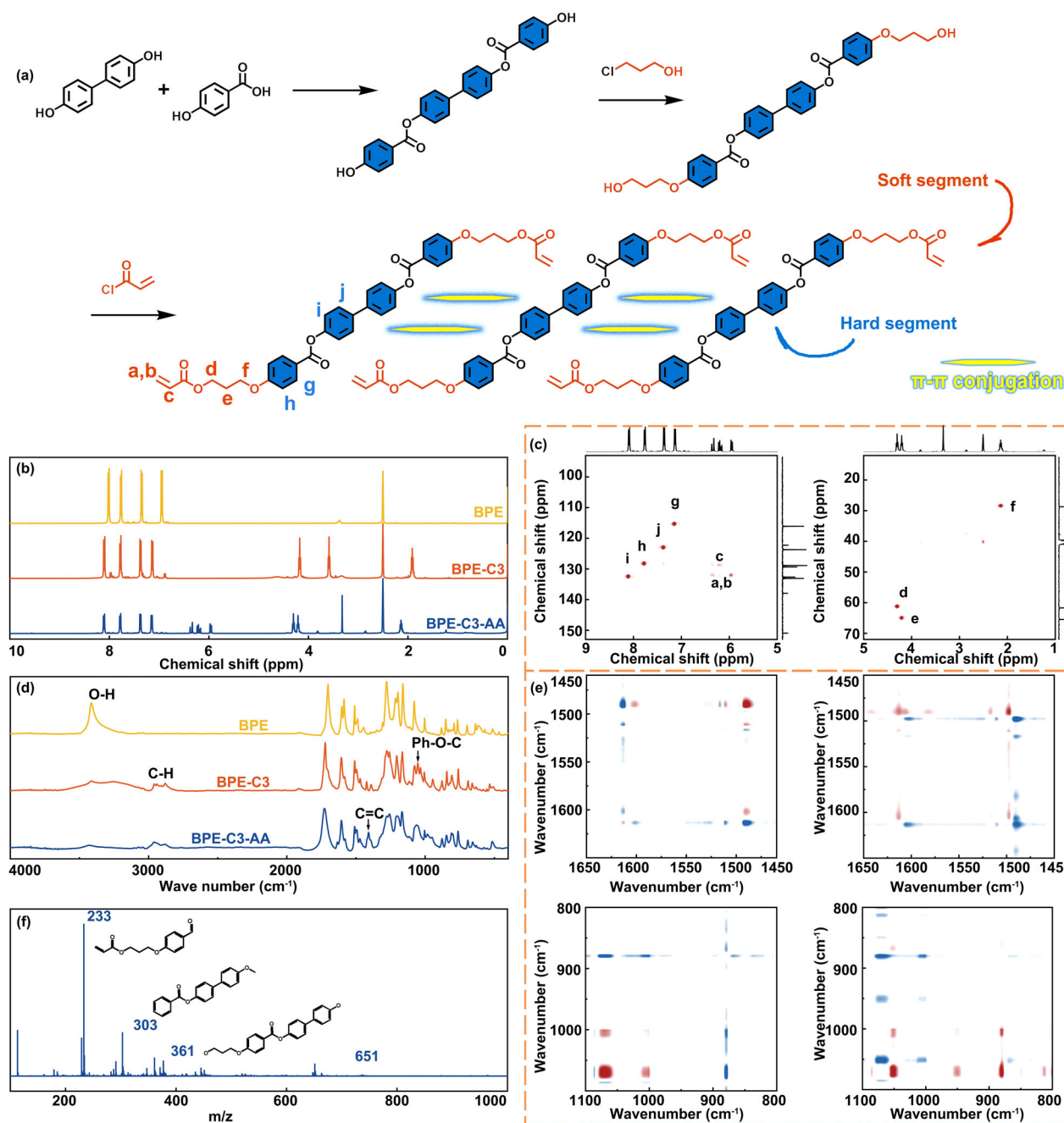


**Fig. 1 | The synthesis of liquid crystal monomer.** **a** The synthesis path of BPE-C3-AA. **b** The  $^1\text{H}$ -NMR spectra of the BPE and its precursor (yellow curve represents BPE, red curve represents BPE-C3, the blue curve represents BPE-C3-AA). **c** The 2D  $^1\text{H}$ - $^{13}\text{C}$  correlated NMR spectra of BPE-C3-AA in different chemical shift ranges.

**d** FTIR spectra of the BPE and its precursor (the yellow curve represents BPE, the red curve represents BPE-C3, the blue curve represents BPE-C3-AA). **e** The 2D FTIR spectra of BPE-C3-AA in different wavenumber ranges. **f** MS of BPE.

under the polarising microscope. This phenomenon indicates the merging of different crystal zones. On a smaller scale, a complete liquid crystal polarising image is given in Fig. 2d. Furthermore, the crystallizability of monomers during the heating and cooling process was studied using XRD. The results are shown in Fig. 2e. Our analysis indicated that the XRD peaks disappeared when the temperature exceeded the melting point, implying that the crystal structure had dissolved at that temperature. However, upon cooling below the melting temperature, the XRD peaks reappeared, suggesting that the crystal structure could be reformed. These results further confirmed the crystallisability of the liquid crystal monomer. The next task is to further align molecules in various crystal zones and fix the structure.

Due to the acrylic ester at the end of the monomer, the monomer gained photopolymerisation properties. In Fig. 2f, two polymerisation paths were given. Details of the process can be found in the experiment section. In the diagram, the blue bars represent the hard segments of the liquid crystal, while the red ribbons represent the soft segments. The hard segments tend to align themselves along the electric field. By applying extra electric field and UV light on the equipment, the orientational molecules can be solidified onto the polymer. SEM reflected the morphology of the sectional view of PBPE-C3-AA-2kV in Fig. 2g, h, which indicates that the sample is homogeneous and solid. From the EDS image shown in Fig. 2i, j, which maps the dispersion of different elements, it can be seen that the material primarily consists of C and O. According to the measured result shown in Table 1, the



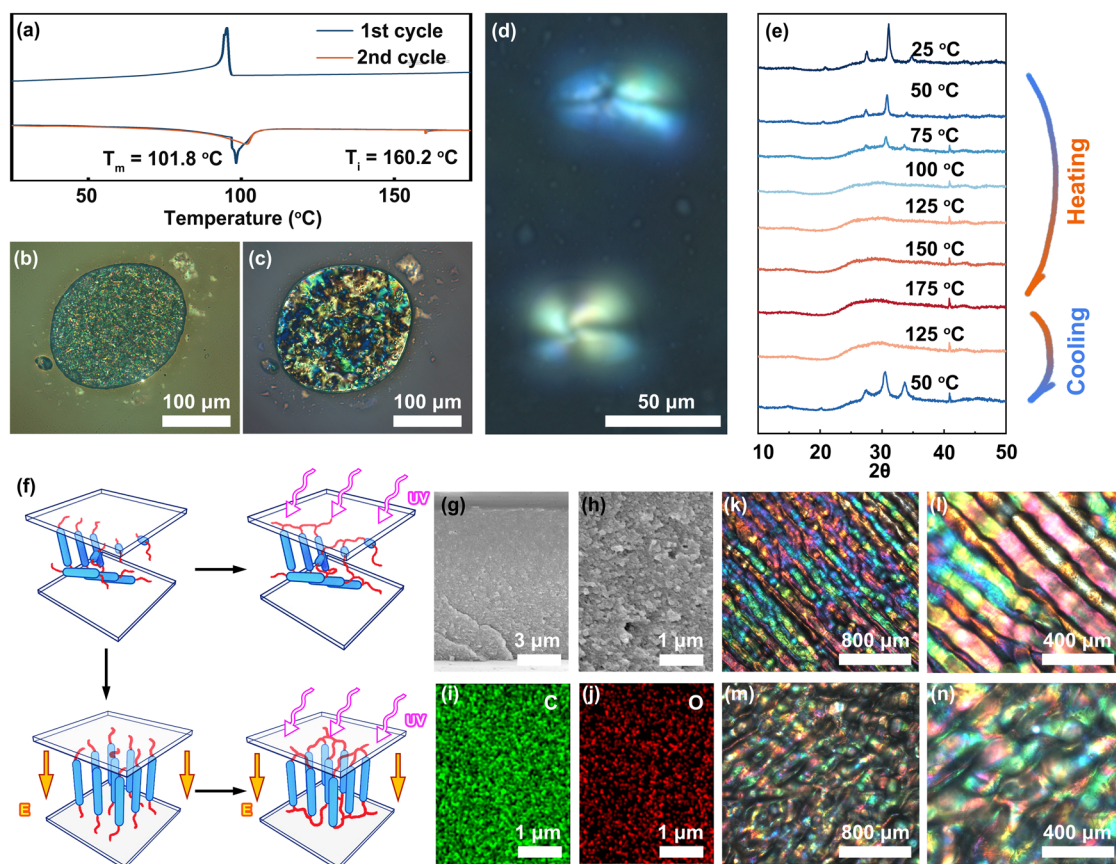


**Fig. 2 | The liquid crystal property of BPE and the schematic diagram of aligning monomers.** **a** The DSC curve of BPE. The blue curve represents the heat absorption and release data of the sample in the first cycle, while the orange curve corresponds to the second cycle. **b** Polarising microscope of BPE at 50 °C. **c, d** Polarising microscope of BPE at 125 °C on different scales. **e** XRD spectrum of BPE during the heating and

cooling process (the warm colour represents high temperature while the cold ones are low temperature). **f** The schematic diagram of aligning monomers. **g, h** SEM image of the sectional view of the sample. **i, j** EDS image of the sectional view. **k, l** Polarising microscope of PBPE-C3-AA at different scale. **m, n** Polarising microscope of PBPE-C3-AA-2kV at different scale.

atomic number density of C to O is about 4, which is close to the calculated value. Figure 2k–n displays polarised images of the resulting polymer at different scales. The first two images were taken from PBPE-C3-AA, while the last two were from PBPE-C3-AA-2kV. In Fig. 2k, m, the crystal is divided into different regions with distinct boundaries. In contrast, the crystal regions tend to form a large connected area in PBPE-C3-AA-2kV, suggesting the presence of an orientational molecule structure.

### Alignment of molecules

This study focuses on the crystallisability of the substance and the orientation of the molecular chains in crystal regions. These structure characters are the result of an extra electric field and the reason for the unique properties of the material. In the electronic field, liquid crystal monomers are aligned, but when the electronic material is withdrawn, the alignment is disturbed. Before polymerisation, the monomer can hardly hold the alignment by itself. So, to solve this, we perform the in situ photopolymerisation to polymerise the monomers under the electronic field. Figure 3a shows a schematic diagram of the crystal region of this liquid crystal polymer. The hard segment of this liquid crystal is composed of conjugated aromatic structures, which tend to form period structures under the assistance of  $\pi$ - $\pi$  interactions. TEM can prove this thought, as shown in Fig. 3b, where the lattice stripes can be observed, and by the electron diffraction spectrum shown in the inset of Fig. 3b.

Because of the close relationship between crystal direction and thermal conductivity, it is worth studying carefully using various methods. The intensity of the Raman peak at  $1283\text{ cm}^{-1}$  corresponds to the covalent bond connecting the two benzene rings in the middle of the molecule parallel to the hard segment, and was measured using polarised Raman spectroscopy at

different scanning angles, as shown in Fig. 3c. The experimental results demonstrate that the Raman scattering intensity of PBPE-C3-AA at  $1283\text{ cm}^{-1}$  is isotropic, indicating that the stiff segment or liquid crystal is not orientational. However, PBPE-C3-AA-2kV exhibits a different behaviour. The Raman scattering intensity in some specific directions becomes stronger than in others, and from a broader perspective, the intensity is closely linked to the incident direction. This phenomenon suggests that the hard segment of the liquid crystal polymer is aligned in a particular direction.

XRD, as introduced, is a powerful tool for investigating crystal structures. Here, SAXS is used to examine the directionality of the crystal region. Within single crystal regions, the polymer chains exhibit order, but their orientations differ between different crystal regions. The intensity of XRD is closely related to the orientation of the crystal regions. When the orientation of the crystal regions is isotropic, the XRD intensity is independent of the incident angle, showing a circular pattern.

On the other hand, if the orientations of the crystal regions are highly aligned, XRD is more intense in certain specific directions, exhibiting a symmetric arc pattern. Figure 3d, e illustrates the diffraction differences between the two structures. The SAXS results of samples solidified with and without an extra electric field are presented in Fig. 3f–i, with the first two figures showing a broad angle range and the latter two a small-angle range. The cycles observed in Fig. 3f, g correspond to the peak at  $21.8^\circ$  in the XRD spectrum, while the ones in Fig. 3h, i correspond to  $2.5^\circ$ . Meanwhile, the scattered ring pattern of the sample made from an extra electric field shows anisotropy and a weaker intensity; the difference may originate from a worse crystallinity or the rotation of crystal orientation. From the comparison between Fig. 3f, g, assuming the worse crystallinity caused it, the intensity of Fig. 3g should also be weaker than Fig. 3f. The phenomenon is not observed;

therefore, the second reason may be dominant. However, more research is required to support the assumption. Due to the use of a copper target with a wavelength of  $1.54 \text{ \AA}$  in the SAXS experiment, the lattice constants corresponding to the two peaks were estimated to be  $4.1 \text{ \AA}$  and  $70.6 \text{ \AA}$ , respectively, which are supposed to be the wide and length of the hard segment as the Fig. 3j shown. It is evident from the spectra that PBPE-C3-AA exhibits isotropic behaviour, while PBPE-C3-AA-2kV displays anisotropic behaviour. It should be noted that while Raman spectra provide information on the chemical bond properties of a material, SAXS spectra, as shown in Fig. 3k, reflect the crystal characteristics.

**Table 1 | The EDS data of carbon and oxygen elements in the LCP**

Elements	Atomic number	Normalised mass (%)	Normalised number of atoms (%)
O	8	25.15	20.15
C	6	74.85	79.85
sum		100	100

Another piece of evidence comes from the fingerprint region of infrared spectra. Infrared spectra describe the asymmetric vibrations of molecules, but the infrared absorptions in the fingerprint region are often difficult to assign and analyse. To solve the problem, Density Functional Theory (DFT) calculations were used to simulate the vibrational modes and dipole moment caused by the vibrations in the fingerprint region of the infrared spectrum. In Fig. 3i, the four vibrations and the direction of their dipole moments calculated for the  $700\text{--}900 \text{ cm}^{-1}$  fingerprint region are labelled. It can be seen that the dipole moment of the  $791 \text{ cm}^{-1}$  vibrational mode is mostly parallel to the liquid crystal molecules, while the other three vibrations are more perpendicular to the molecules. When infrared light passes through a substance, the angle between the dipole moment direction and the infrared light can affect its absorption intensity. By comparing with the calculated spectrum shown in Fig. 3m, the specific infrared absorption can be recognised in Fig. 3n, which presents measured spectra. It can be seen that the extra electric field can change the strength of infrared absorption with dipole moments perpendicular to molecular slightly while changing the strength of parallel one significantly. Figure 3o displays the area ratio of the specific peaks between PBPE-C3-AA and PBPE-C3-AA-2kV. From the comparison, we can see that the area ratios at  $772$ ,  $835$  and  $877 \text{ cm}^{-1}$  are  $0.7\text{--}1.1$ , while the ratios at  $791 \text{ cm}^{-1}$  are  $1.9$ . This phenomenon suggests that the applied electric field can only cause molecules to rotate around an axis

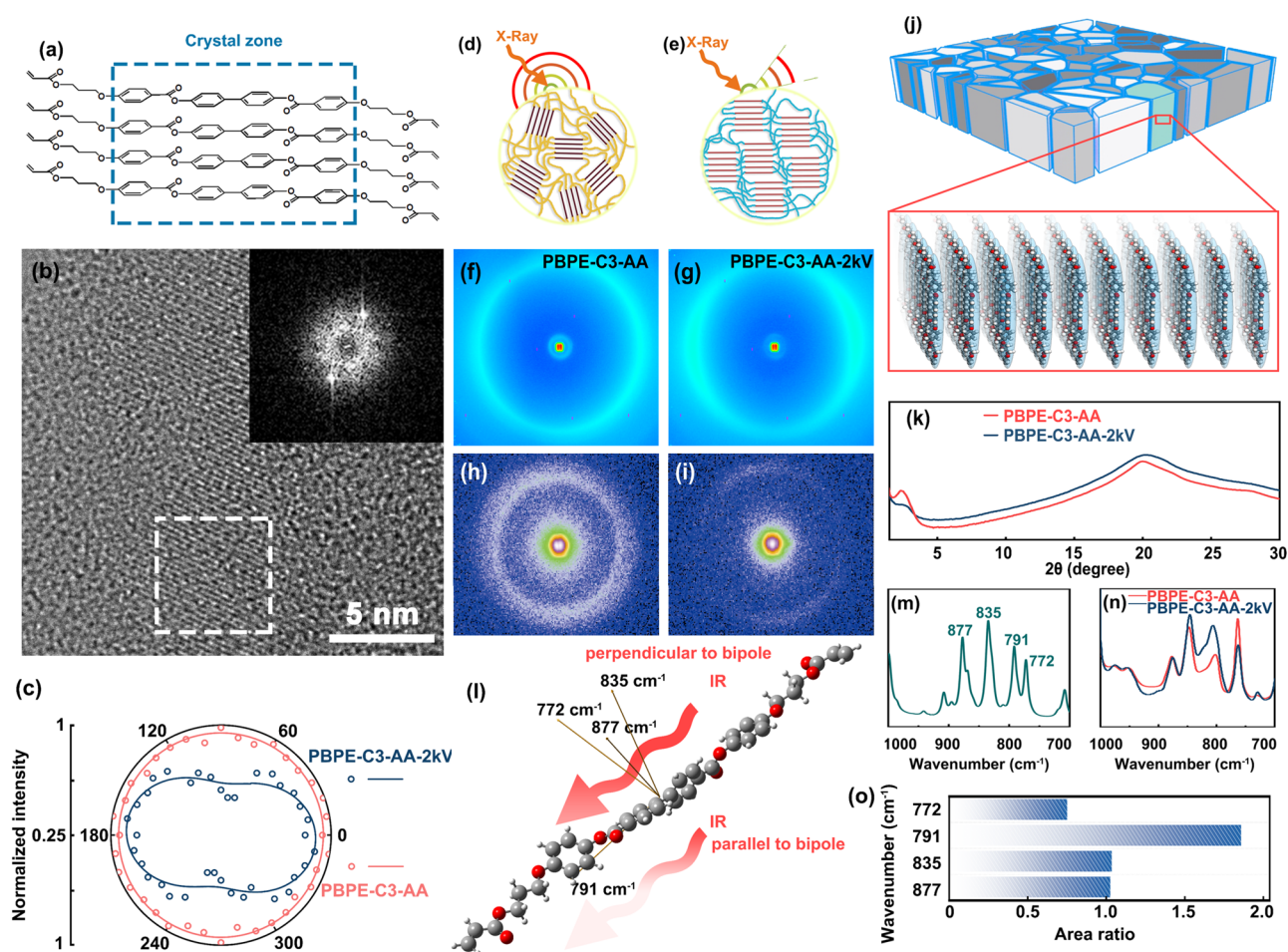


**Fig. 3 | Confirmation of liquid crystal polymer under electric field. a** diagram of crystal monomer under electric field. **b** The TEM of PBPE-C3-AA where the hard segment was marked. **c** Polarising RAMAN spectrum of liquid crystal polymers which were synthesised with and without electronic field (the dots are measured results and curves are fitted, blue ones represent PBPE-C3-AA-2kV while red ones represent PBPE-C3-AA). **d** X-ray reflection schematic of liquid crystal polymers with disordered crystal region. **e** X-ray reflection schematic of liquid crystal polymers with oriented crystal region. **f, g** WAXS spectra of PBPE-C3-AA and PBPE-C3-AA-2kV. **h, i** SAXS spectra of PBPE-C3-AA and PBPE-C3-AA-2kV. **j** A schematic of crystal zone and the molecular in them. **k** XRD spectrum of samples. (blue curve represents PBPE-C3-AA-2kV and the red one represents PBPE-C3-AA). **l** Relationship of IR absorption and the direction of dipole moment. **m** FTIR calculated from DFT calculation. **n** The measured FTIR of samples in the fingerprint region (blue curve represents PBPE-C3-AA-2kV and the red one represents PBPE-C3-AA). **o** The area ratio of the specific peaks between PBPE-C3-AA and PBPE-C3-AA-2kV.

AA-2kV. **h, i** SAXS spectra of PBPE-C3-AA and PBPE-C3-AA-2kV. **j** A schematic of crystal zone and the molecular in them. **k** XRD spectrum of samples. (blue curve represents PBPE-C3-AA-2kV and the red one represents PBPE-C3-AA). **l** Relationship of IR absorption and the direction of dipole moment. **m** FTIR calculated from DFT calculation. **n** The measured FTIR of samples in the fingerprint region (blue curve represents PBPE-C3-AA-2kV and the red one represents PBPE-C3-AA). **o** The area ratio of the specific peaks between PBPE-C3-AA and PBPE-C3-AA-2kV.



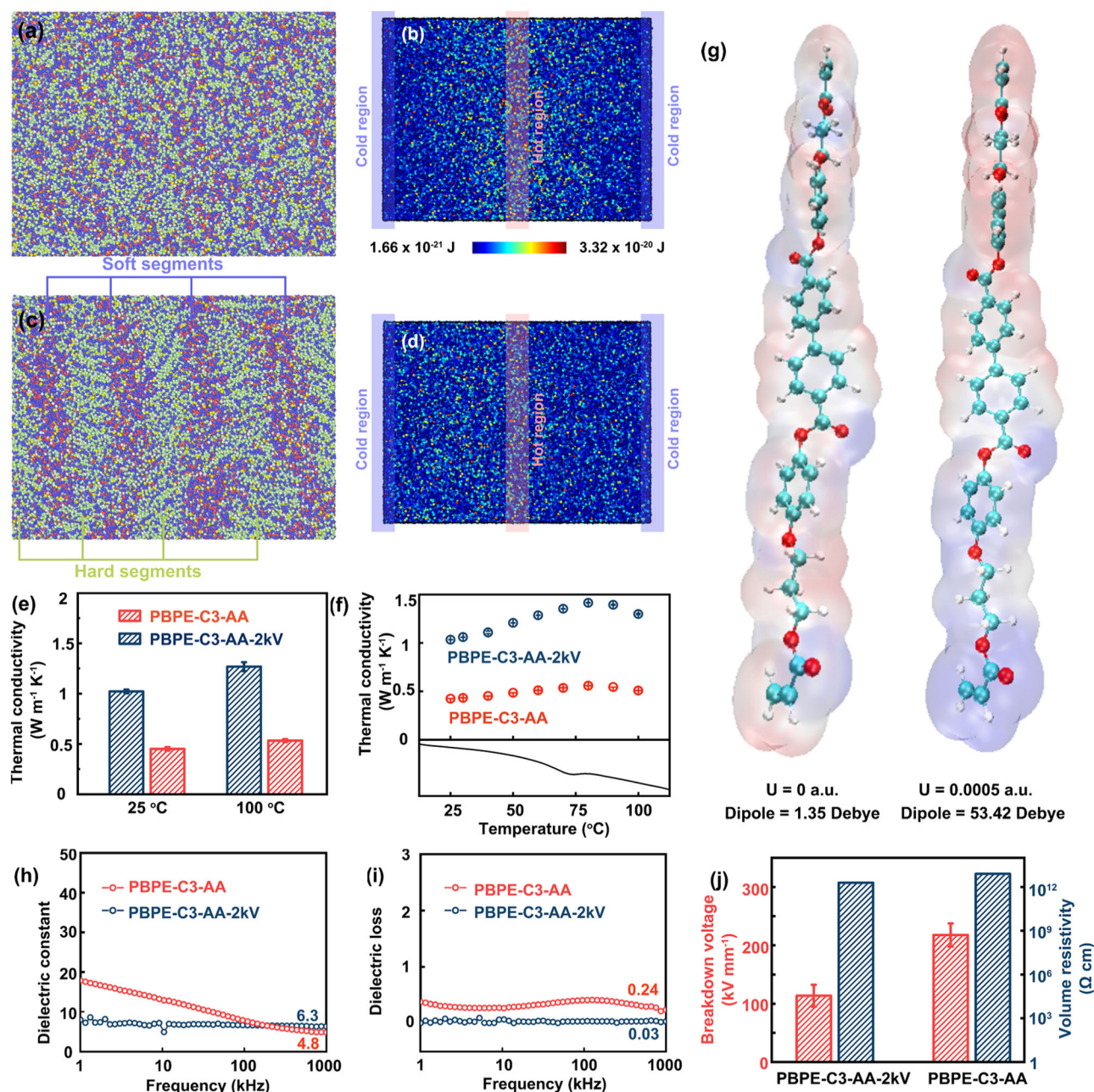


**Fig. 4 | The thermal and electrical properties of LCP.** **a** The structure of PBPE-C3-AA. **b** The kinetic energy of atom in PBPE-C3-AA in NEMD process. **c** The structure of PBPE-C3-AA-2kV. **d** The kinetic energy of atom in PBPE-C3-AA-2kV in NEMD process. **e** The thermal conductivity of samples at different temperature (blue column represents PBPE-C3-AA-2kV and the red one represents PBPE-C3-AA). **f** The thermal conductivity of samples during heating process and the DSC curve of polymer in the same temperature range (blue curve represents PBPE-C3-AA-2kV

and the red one represents PBPE-C3-AA). **g** The electron distribution analysis and the dipole moment of monomer. **h** Dielectric constant of samples (blue dots represent PBPE-C3-AA-2kV and the red one represent PBPE-C3-AA). **i** Dielectric loss of samples (blue dots represent PBPE-C3-AA-2kV and the red one represent PBPE-C3-AA). **j** Breakdown voltage and volume resistivity of samples (blue column represents volume resistivity and the red one represents breakdown voltage).

perpendicular to the molecule but cannot modulate the precise spatial orientation of the molecule.

### Property of polymer

We used the DFT method to calculate the spatial charge distribution and colour-coded the surroundings of the LC molecule based on it. The results are shown in Fig. 4. The blue regions represent a denser electron cloud distribution, while the red areas indicate a higher concentration of positive charge. In addition, the figure displays the overall molecular dipole moment.

Up to now, the crystallinity and the alignment of molecular or crystal regions have been discussed. Here, we characterised the influence of the

alignment on thermal conductivity. First of all, molecular dynamics (MD) was used to simulate the heat transport in different structures. MD simulation was performed with the Lammmps package<sup>42</sup>. In Fig. 4a, c, the structure of disordered and aligned liquid crystal polymer is shown. 255 polymer chains, each containing 4 monomers, were put in a  $100 \times 100 \times 100$  Å box. OPLS force field was employed to simulate the liquid crystal monomers<sup>43</sup>. Atoms were coloured to distinguish them from each other. The red ones are the carbon atoms of soft segments, while the green ones are the carbon atoms of hard segments. The blue ones are hydrogen atoms attached to the main chain. In Fig. 4a, we can observe the disorder atoms, while in Fig. 4c, the outline of hard and soft segments can be seen. In the simulation, the time

step is 0.1 fs. The heat was injected in the box at the mid part and extracted at the left and the right parts, labelled in Fig. 4b, d. The heat flux is  $1 \text{ kcal mol}^{-1} \text{ fs}^{-1}$ . After the 120 ps simulation, we sampled the velocity of each atom. Considering that kinetic energy can be calculated by

$$E = \frac{3}{2} kT = \frac{1}{2} mv^2 \quad (1)$$

where  $k$ ,  $T$ ,  $m$  and  $v$  are Boltzmann constants, temperature, mass, and atom velocity, respectively. From Eq. (1), we can see that the temperature can be expressed from the velocity. In Fig. 4b, d, the atoms were coloured by their kinetic energy. The lighter the colour is, the faster the atom moves and, therefore, the higher the temperature is. Here, the temperature of the hot region rises faster in the PBPE-C3-AA system than in the PBPE-C3-AA-2kV one, which is attributed to the difference in heat transport speed between the two structures.

Then, the thermal conductivity was measured with a laser flash apparatus (LFA) and shown in Fig. 4e. At room temperature, compared with PBPE-C3-AA, the thermal conductivity of PBPE-C3-AA-2kV is doubled and reached  $1.02 \text{ W m}^{-1} \text{ K}^{-1}$ . This value is outstanding among most polymers. On the contrary, if the external field does not appear, the thermal conductivity of PBPE-C3-AA is only  $0.45 \text{ W m}^{-1} \text{ K}^{-1}$ . The standard deviations of the two samples obtained from the three tests are 0.018 and  $0.017 \text{ W m}^{-1} \text{ K}^{-1}$ , respectively. When the temperature is raised to  $100^\circ \text{C}$ , the thermal conductivity of PBPE-C3-AA-2kV and PBPE-C3-AA can grow to 1.26 and  $0.53 \text{ W m}^{-1} \text{ K}^{-1}$ , respectively. Figure 4f shows the influences of the temperature on thermal conductivity. With the rise in temperature, the thermal conductivity first increases and then falls down. Comparing the transition temperature of thermal conductivity and the DSC curve in the same temperature range, it can be found that the transition temperature of thermal conductivity is close to the onset temperature on the DSC curve, which indicates that the change in the trend of thermal conductivity may be related to the phase transition.

In previous studies, researchers have pointed out that LCP exhibits excellent electrical properties due to its unique energy band structure<sup>44</sup>. Here, we studied the electrical properties of LCP and its monomer. The electron distribution of monomers under different conditions was studied first because it may be the reason for the molecular aligning in an electric field. We used the DFT method to calculate the Mulliken charge distribution. We coloured the surroundings of the LC molecule according to the results, as shown in Fig. 4g. The blue regions represent electron cloud distribution. In contrast, the red regions indicate a higher concentration of positive charge. The first picture is the charge distribution without an extra electric field. In this situation, the electron distribution is primarily influenced by atomic electronegativity and conjugated structures. The second one shows the charge distribution surrounding the monomer under a  $0.0005 \text{ a.u.}$  extra electric field. Under the influence of an external electric field, the positive and negative charges within the molecule are separated to form distinct positive and negative charge centres, and the dipole moment rises from 1.35 to 53.42 Debye. The positive and negative charge centres are individually subjected to the influence of the electric field, leading to the development of an orientation tendency of the molecule along the direction of the electric field.

The dielectric constant and dielectric loss of PBPE-C3-AA and PBPE-C3-AA-2kV at different electromagnetic wave frequencies are shown in Fig. 4h, i. According to the measurement, the dielectric constant increased from 4.8 to 6.3 at 1000 kHz when the extra electric field was applied to the sample during preparation. The difference is resourced from the alignment of the hard segment. When exposed to an electric field, an aligned conjugate structure provides a larger potential dipole moment length. Considering that the dipole moment can be calculated by

$$P = qr \quad (2)$$

Where  $q$  and  $r$  are charge and dipole moment length. This formula indicates the dipole moment increases with  $q$  and  $r$ . Considering the chemical structure remains, the difference of excited charge in the electric field should be comparable, so the dipole moment length is the major influence of the dipole moment. Meanwhile

$$P = \varepsilon_0 (\varepsilon_r - 1) E \quad (3)$$

where  $\varepsilon_0$ ,  $\varepsilon_r$  and  $E$  represent the dielectric constant of free space, relative dielectric constant and extra electric field strength. The formula indicates that when a material is exposed to a constant electric field, the dipole moment is proportional to its dielectric constant. As a result, the longer dipole moment length may be the reason for the higher dielectric constant. Meanwhile, the dielectric loss of the two samples is lower than 1, as shown in Fig. 4i. The value of PBPE-C3-AA-2kV is even lower than 0.1, which is 1 more order of magnitude smaller than PBPE-C3-AA.

The breakdown voltage and volume resistivity of samples are given in Fig. 4j. The breakdown voltage of PBPE-C3-AA-2kV is  $113 \text{ kV mm}^{-1}$ , which is only half of the value of PBPE-C3-AA,  $217 \text{ kV mm}^{-1}$ . The volume resistivity of the two samples is similar to each other, both of which are about  $10^{12} \Omega \text{ cm}$ . This value indicates that the material is a kind of insulator.

## Conclusion

In summary, a monomer BPE-C3-AA was designed and synthesised to possess an ability to photopolymerisation and electric-responsibility. The liquid crystal properties are studied with a polarising microscope and DSC. The phase change temperature of the monomer is  $101.8$  and  $160.2^\circ \text{C}$ , respectively. We fabricated a liquid crystal polymer with a through-plane thermal conductivity of  $1.02 \text{ W m}^{-1} \text{ K}^{-1}$  by in situ photopolymerising the BPE-C3-AA monomer under a  $2 \text{ kV}$  extra electronic field. From the results of the experiments, the alignment of the segments can be confirmed. The relationship between the alignment condition of the liquid crystal segments and thermal conductivity was studied with molecular dynamic simulations. Our PBPE-C3-AA-2kV is one of the best thermal conductive examples of liquid crystal polymers, with excellent electrical properties and thermal stability; thus, it is supposed to have a profound influence on thermal management materials.

## Methods

### Materials

*p*-Hydroxybenzoic acid, 4,4'-dihydroxydiphenyl, 3-chloro-1-propanol, *p*-toluenesulfonic acid monohydrate, triethylamine, sodium iodide, diphenyl(2,4,6-trimethylbenzoyl) (TPO), acryloyl chloride, *N,N*-dimethylacetamide, xylenes, and 2-butanone were purchased from Shanghai Aladdin Biochemical Technology Co., Ltd. 2-Butanone was purchased from Sino-pharm Chemical Reagent Co., Ltd.

### Synthesis of BPE

In total,  $10 \text{ g}$  of *p*-Hydroxybenzoic acid,  $6.74 \text{ g}$  of 4,4'-dihydroxydiphenyl and  $0.5 \text{ g}$  of *p*-toluenesulfonic acid monohydrate were dissolved in  $80 \text{ mL}$  of xylenes, and the mixture was heated at  $160\text{--}165^\circ \text{C}$  for  $24 \text{ h}$ . The reaction was conducted in a flask equipped with a magnetic stirrer and Dean-Stark trap. The compound was filtered using a Buchner funnel, and the precipitate was dried at  $70^\circ \text{C}$  and labelled as BPE.

### Synthesis of BPE-C3

In total,  $8.5 \text{ g}$  of BPE,  $5 \text{ mL}$  of 3-chloro-1-propanol,  $6.4 \text{ g}$  of sodium iodide (NaI), and  $2 \text{ g}$  of sodium hydroxide (NaOH) were dissolved in  $80 \text{ mL}$  of 2-butanone. The mixture was heated to  $60^\circ \text{C}$  and stirred for  $72 \text{ h}$ . The resulting product was poured into ice-cold deionised water to quench the reaction. The solution was filtered using a Buchner funnel, and the precipitate, labelled as BPE-C3, was dried at  $70^\circ \text{C}$  and collected.



## Synthesis of BPE-C3-AA

A nitrogen-filled flask was used to prevent the influence of moisture in the air. In all, 35 mL of dry N and N-dimethylacetamide were injected into the flask, and 2.7 g of BPE-C3 was added under nitrogen protection. The solution was cooled in an ice water bath. At 0 °C, 1.1 mL of triethylamine was added to remove the generated HCl. Then, 2 mL of acryloyl chloride was slowly added to the flask over 10 min. After 30 min, the ice water bath was removed, and the flask was immediately covered with aluminised paper. The reaction was allowed to proceed for 8 h. The solution was then poured into ice water to quench the reaction, filtered, and the resulting precipitate, labelled BPE-C3-AA, was dried at 70 °C.

## Synthesis of PBPE-C3-AA and PBPE-C3-AA-2kV

BPE-C3-AA was heated to 135 °C. 10 wt% of TPO was used as an initiator. The solution was applied onto a conductive substrate which is heated to 135 °C. An indium tin oxide (ITO) was covered on the sample. There is a 1 mm space left between the substrate and ITO. The voltage between the substrate and ITO was set at different values. Then, the monomer is solidified using 365 nm UV light through the ITO. If the voltage between the substrate and ITO is 0 V, the resulting sample is labelled PBPE-C3-AA, while the voltage is 2 kV, and the resulting sample is PBPE-C3-AA-2kV.

## Measurement and characterisation

The chemical structures of the precursors and resulting monomer were investigated using <sup>1</sup>H nuclear magnetic resonance (NMR) spectroscopy, 2D <sup>1</sup>H-<sup>13</sup>C correlated NMR spectroscopy, and Fourier transform infrared spectroscopy (FTIR). The NMR spectra were obtained using a Bruker AVANCE NEO 400 MHz instrument, with dimethyl sulfoxide (DMSO) as the solvent. The chemical shift of the solvent on the <sup>1</sup>H-NMR spectrum was measured at 2.50 ppm, while the chemical shift of water in the solvent was observed at 3.38 ppm. FTIR spectra of these compounds were obtained using a Thermo Fisher IS50 instrument. The mass spectrum (MS) of BPE-C3-AA was recorded using an AB Sciex 4600 mass spectrometer.

To confirm the liquid crystal properties, differential scanning calorimetry (DSC) measurements of the monomer, BPE-C3-AA, were performed using a TA DSC 2500 calorimeter. Polarised images of the monomer during the heating process were captured using a polarising microscope; the angle position of the polariser is fixed at 90°. X-ray diffraction (XRD) spectra at different temperatures were obtained using a Bruker ADVANCE D8 X-ray diffractometer.

After polymerisation, the morphology and energy dispersive spectroscopy (EDS) were observed with a polarising microscope and HITACHI 8230 scanning electron microscopy (SEM). The crystal structure of the polymer was confirmed using various techniques, including transmission electron microscopy (TEM) with a Thermo Fisher Talos F200X instrument, polarised Raman spectroscopy with a Horiba LabRAM HR Evolution instrument, Small-Angle X-ray Scattering (SAXS) with XENOCs SAS Xeuss 3.0 UHR, and FTIR spectroscopy.

The thermal and electrical properties of the material were thoroughly investigated. The thermal conductivity was calculated using the following formula,

$$K = \alpha C_p \rho \quad (4)$$

where  $\alpha$  represents thermal diffusivity,  $C_p$  represents specific heat, and  $\rho$  represents density. To measure the thermal diffusivity and specific heat, a laser flash apparatus (LFA; Netzsch LFA 467, Germany) and a differential scanning calorimeter (DSC) were employed, respectively. The density of the material was determined using the Archimedes principle in conjunction with a balance. The samples in this manuscript are polymerised from liquid crystal monomer between two electrodes spaced 1 mm apart. So, the thickness of resulted polymer is around 1 mm. The diameter is about 8–20 mm which can be adjusted by the amount of monomer. The sample

size meets the requirements specified by LFA, so testing can be conducted after a simple cleaning and cutting process. The permittivity, dielectric loss and electric breakdown strength of samples were measured with home-made equipment.

## Data availability

The datasets generated during and/or analysed during the current study are available from the corresponding author upon reasonable request.

Received: 24 November 2023; Accepted: 30 January 2024;

Published online: 21 February 2024

## References

- Jing, L. et al. 3D Graphene-Nanowire “Sandwich” Thermal Interface with Ultralow Resistance and Stiffness. *ACS Nano* **17**, 2602–2610 (2023).
- Zhang, N. et al. Improving the interlaminar bonding and thermal conductivity of polymer composites by using split-radial mesophase pitch-based carbon fiber as reinforcement. *Compos. Part B Eng.* **252**, 110509 (2023).
- Ge, X. et al. Flexible and leakage-proof phase change composite for microwave attenuation and thermal management. *Carbon* **210**, 118084 (2023).
- Huang, T. et al. Self-modifying nanointerface driving ultrahigh bidirectional thermal conductivity boron nitride-based composite flexible films. *Nano-Micro Lett.* **15**, 2 (2022).
- Li, M. et al. Epoxy composite with metal-level thermal conductivity achieved by synergistic effect inspired by lamian noodles. *Compos. Sci. Technol.* **228**, 109677 (2022).
- Wang, D., Liu, D., Xu, J., Fu, J. & Wu, K. Highly thermoconductive yet ultraflexible polymer composites with superior mechanical properties and autonomous self-healing functionality via a binary filler strategy. *Mater. Horizons* **9**, 640–652 (2022).
- Chen, Y. et al. Thermally conductive but electrically insulating polybenzazole nanofiber/boron nitride nanosheets nanocomposite paper for heat dissipation of 5G base stations and transformers. *ACS Nano* **16**, 14323–14333 (2022).
- Peng, L. et al. Ultrahigh thermal conductive yet superflexible graphene films. *Adv. Mater.* **29**, 1700589 (2017).
- Tao, K. et al. Structural design and research progress of thermally conductive polyimide film—a review. *Macromol. Rapid Commun.* **44**, 2300060 (2023).
- Ruan, K. et al. Electric-field-induced alignment of functionalized carbon nanotubes inside thermally conductive liquid crystalline polyimide composite films. *Angew. Chem. Int. Ed.* **62**, e202309010 (2023).
- Pan, X., Debije, M. G. & Schenning, A. P. H. J. High thermal conductivity in anisotropic aligned polymeric materials. *ACS Appl. Polymer Mater.* **3**, 578–587 (2021).
- Liu, J. & Yang, R. Length-dependent thermal conductivity of single extended polymer chains. *Phys. Rev. B* **86**, 104307 (2012).
- Hu, G.-J., Cao, B.-Y. & Li, Y.-W. Thermal conduction in a single polyethylene chain using molecular dynamics simulations. *Chinese Phys. Lett.* **31**, 086501 (2014).
- Wang, X., Ho, V., Segalman, R. A. & Cahill, D. G. Thermal conductivity of high-modulus polymer fibers. *Macromolecules* **46**, 4937–4943 (2013).
- Shen, S., Henry, A., Tong, J., Zheng, R. & Chen, G. Polyethylene nanofibres with very high thermal conductivities. *Nat. Nanotechnol.* **5**, 251–255 (2010).
- Xu, Y. et al. Nanostructured polymer films with metal-like thermal conductivity. *Nat. Commun.* **10**, 1771 (2019).
- Chen, X. et al. Tropocollagen-inspired hierarchical spiral structure of organic fibers in epoxy bulk for 3D high thermal conductivity. *Adv. Mater.* **34**, 2206088 (2022).
- Zhang, Y., Lei, C., Wu, K. & Fu, Q. Fully Organic bulk polymer with metallic thermal conductivity and tunable thermal pathways. *Adv. Sci.* **8**, 2004821 (2021).



19. Liu, Y. et al. Polymer films with metal-like thermal conductivity, excellent stability, and flame retardancy. *Adv. Funct. Mater.* **33**, 2303561 (2023).
20. Ruan, K., Zhong, X., Shi, X., Dang, J. & Gu, J. Liquid crystal epoxy resins with high intrinsic thermal conductivities and their composites: a mini-review. *Mater. Today Phys.* **20**, 100456 (2021).
21. Fan, X., Liu, Z., Wang, S. & Gu, J. Low dielectric constant and highly intrinsic thermal conductivity fluorine-containing epoxy resins with ordered liquid crystal structures. *SusMat* **3**, 877–893 (2023).
22. Zhong, X., Ruan, K. & Gu, J. Enhanced thermal conductivities of liquid crystal polyesters from controlled structure of molecular chains by introducing different dicarboxylic acid monomers. *Research* **2022**, 1–11 (2022).
23. Tian, R. et al. Flexible, flame-resistant, and anisotropic thermally conductive aerogel films with ionic liquid crystal-armed boron nitride. *ACS Appl. Mater. Interfaces* **15**, 27223–27233 (2023).
24. Yeo, H. et al. Characteristic correlation between liquid crystalline epoxy and alumina filler on thermal conducting properties. *Compos. Sci. Technol.* **141**, 99–105 (2017).
25. Harada, M., Hamaura, N., Ochi, M. & Agari, Y. Thermal conductivity of liquid crystalline epoxy/BN filler composites having ordered network structure. *Compos. Part B Eng.* **55**, 306–313 (2013).
26. Hammerschmidt, A., Geibel, K. & Strohmer, F. In situ photopolymerized, oriented liquid-crystalline diacrylates with high thermal conductivities. *Adv. Mater.* **5**, 107–109 (1993).
27. Ahlers, G., Cannell, D. S., Berge, L. I. & Sakurai, S. Thermal conductivity of the nematic liquid crystal 4-n-pentyl-4'-cyanobiphenyl. *Phys. Rev. E* **49**, 545–553 (1994).
28. Marinelli, M., Mercuri, F., Foglietta, S., Zammit, U. & Scudieri, F. Anisotropic heat transport in the octylcyanobiphenyl (8CB) liquid crystal. *Phys. Rev. E* **54**, 1604–1609 (1996).
29. Lv, G. et al. Odd–even effect on the thermal conductivity of liquid crystalline epoxy resins. *Proc. Natl. Acad. Sci. USA* **119**, e2211151119 (2022).
30. Ruan, K., Guo, Y. & Gu, J. Liquid crystalline polyimide films with high intrinsic thermal conductivities and robust toughness. *Macromolecules* **54**, 4934–4944 (2021).
31. Deng, S. et al. Electric-field-induced modulation of thermal conductivity in poly(vinylidene fluoride). *Nano Energy* **82**, 105749 (2021).
32. Kim, Y. H. et al. Optically selective microlens photomasks using self-assembled smectic liquid crystal defect arrays. *Adv. Mater.* **22**, 2416–2420 (2010).
33. Xu, Y. et al. Molecular engineered conjugated polymer with high thermal conductivity. *Sci. Adv.* **4**, eaar3031 (2018).
34. Ruan, K. & Gu, J. Ordered alignment of liquid crystalline graphene fluoride for significantly enhancing thermal conductivities of liquid crystalline polyimide composite films. *Macromolecules* **55**, 4134–4145 (2022).
35. Li, Y. et al. Flexible epoxy-dispersed liquid crystal membranes of intrinsic thermal conductivity with high voltage orientation molding. *J. Appl. Polymer Sci.* **139**, e53077 (2022).
36. Wu, Y. et al. High thermal conductivity and excellent mechanical properties of liquid crystal co-polyester based on hydron bond. *J. Appl. Polymer Sci.* **140**, e53951 (2023).
37. Li, Y. et al. Liquid crystalline texture and hydrogen bond on the thermal conductivities of intrinsic thermal conductive polymer films. *J. Mater. Sci. Technol.* **82**, 250–256 (2021).
38. Zhong, X. et al. Discotic liquid crystal epoxy resins integrating intrinsic high thermal conductivity and intrinsic flame retardancy. *Macromol. Rapid Commun.* **43**, 2100580 (2022).
39. Liu, B. et al. Switching plastic crystals of colloidal rods with electric fields. *Nat. Commun.* **5**, 3092 (2014).
40. Li, B.-X. et al. Electrically driven three-dimensional solitary waves as director bullets in nematic liquid crystals. *Nat. Commun.* **9**, 2912 (2018).
41. Yonehara, T., Hayashi, H., Nimori, S. & Goto, H. Vapor treatment, liquid crystal formation, magnetic orientation, and crystallization (VLMC) to form helical polyisocyanides with oriented crystal-like structure. *J. Appl. Polymer Sci.* **137**, 49408 (2020).
42. Thompson, A. P. et al. LAMMPS—a flexible simulation tool for particle-based materials modeling at the atomic, meso, and continuum scales. *Comput. Phys. Commun.* **271**, 108171 (2022).
43. Yabe, M., Mori, K., Ueda, K. & Takeda, M. Development of PolyParGen software to facilitate the determination of molecular dynamics simulation parameters for polymers. *J. Comput. Chem.* **5**, 2018–0034 (2019).
44. Chen, J. et al. Ladderphane copolymers for high-temperature capacitive energy storage. *Nature* **615**, 62–66 (2023).

## Acknowledgements

The authors are grateful for the financial support from the Science and Technology Base and Talent Project of Guangxi (2022AC16005) and the National Natural Science Foundation of China (51573201, 52075527 and U1709205). We are also grateful for access to the University of Nottingham Ningbo China High-Performance Computing Facility.

## Author contributions

Maohua Li: lead the writing of original draft, lead the experiment design. Ping Gong: lead experiment performance. Zhenbang Zhang: lead formal analysis. Linhong Li: lead data curation Yapeng Chen: equal draft edit. Yue Qin: lead calculation and simulation. Yingying Guo: equal experiment performance. Rongjie Yang: supporting experiment performance. Jianxinag Zhang: supporting simulation. Yiwei Zhou: supporting draft edit. Kang Xu: supporting experiment design. Yandong Wang: lead validation. Hainan Do: equal calculation and simulation. Xiaofei Jia: supporting synthesis. Tao Cai: supporting project administration. Cheng-Te Lin: supporting project administration. Nan Jiang: lead funding acquisition. Jinhong Yu: equal funding acquisition.

## Competing interests

The authors declare no competing interests.

## Additional information

**Correspondence** and requests for materials should be addressed to Nan Jiang or Jinhong Yu.

**Peer review information** *Communications Materials* thanks Junwei Gu and the other, anonymous, reviewer(s) for their contribution to the peer review of this work. Primary Handling Editors: Jet-Sing Lee.

**Reprints and permissions information** is available at <http://www.nature.com/reprints>

**Publisher's note** Springer Nature remains neutral with regard to jurisdictional claims in published maps and institutional affiliations.

**Open Access** This article is licensed under a Creative Commons Attribution 4.0 International License, which permits use, sharing, adaptation, distribution and reproduction in any medium or format, as long as you give appropriate credit to the original author(s) and the source, provide a link to the Creative Commons license, and indicate if changes were made. The images or other third party material in this article are included in the article's Creative Commons license, unless indicated otherwise in a credit line to the material. If material is not included in the article's Creative Commons license and your intended use is not permitted by statutory regulation or exceeds the permitted use, you will need to obtain permission directly from the copyright holder. To view a copy of this license, visit <http://creativecommons.org/licenses/by/4.0/>.

© The Author(s) 2024